



Universidad Autónoma  
de Madrid

**Biblos-e Archivo**  
Repositorio Institucional UAM

**Repositorio Institucional de la Universidad Autónoma de Madrid**

<https://repositorio.uam.es>

Esta es la **versión de autor** del artículo publicado en:

This is an **author produced version** of a paper published in:

Solar Energy 205 (2020): 154-160

**DOI:** <https://doi.org/10.1016/j.solener.2020.05.043>

**Copyright:** © 2020 International Solar Energy Society. Published by Elsevier Ltd. All rights reserved. This manuscript version is made available under the CC-BY-NC-ND 4.0 licence <http://creativecommons.org/licenses/by-nc-nd/4.0/>

El acceso a la versión del editor puede requerir la suscripción del recurso

Access to the published version may require subscription

# Raman mapping of MoS<sub>2</sub> at Cu<sub>2</sub>ZnSnS<sub>4</sub>/Mo interface in thin film

I.S. Babichuk <sup>a,b</sup>, M.O. Semenenko <sup>b</sup>, R. Caballero <sup>c</sup>, O.I. Datsenko <sup>d</sup>, S. Golovynskyi <sup>e</sup>,  
Ran Qiu <sup>e</sup>, Chun Huang <sup>e</sup>, Rui Hu <sup>e</sup>, I.V. Babichuk <sup>f</sup>, R.R. Ziniuk <sup>e</sup>, M. Stetsenko <sup>b,e</sup>,  
O.A. Kapush <sup>b</sup>, Jian Yang <sup>a,\*</sup>; Baikui Li <sup>e,\*</sup>, Junle Qu <sup>e,\*</sup>, M. Leon <sup>c</sup>

<sup>a</sup> Faculty of Intelligent Manufacturing, Wuyi University, 529020, Jiangmen, P. R. China

<sup>b</sup> V. Lashkaryov Institute of Semiconductor Physics, NAS of Ukraine, 03680, Kyiv, Ukraine

<sup>c</sup> Universidad Autónoma de Madrid, Departamento de Física Aplicada, 28049 Madrid, Spain

<sup>d</sup> Physics Department, Taras Shevchenko National University of Kyiv, 01601, Kyiv, Ukraine

<sup>e</sup> Key Laboratory of Optoelectronic Devices and Systems of Ministry of Education and Guangdong Province, College of Physics and Optoelectronic Engineering, Shenzhen University, 518060, Shenzhen, P.R. China

<sup>f</sup> National Center “Minor academy of sciences of Ukraine”, 04119, Kyiv, Ukraine

\*Corresponding authors:

E-mail addresses: jianyang@szu.edu.cn; libk@szu.edu.cn; jlqu@szu.edu.cn

## Abstract

A Cu<sub>2</sub>ZnSnS<sub>4</sub> (CZTS) thin film deposited on Mo contact film using direct current magnetron sputtering and sulfurized is studied. The morphological and structural investigations are focused on the interface between CZTS and back Mo layer. The film is shown to be polycrystalline with an average grain size of 0.8 μm and of a high conductivity of the grain boundaries. It is also characterized by a suitable elemental composition with a noncritical deviation from the stoichiometry across the film depth. This results in the optical bandgap of 1.48 eV which is optimal for solar cell absorbers. Raman spectra show low FWHMs of two A-symmetry dominant bands for CZTS thin film, which confirms high quality of crystal structure over large area. At the same time, ZnS secondary phase is found on the film surface, while MoS<sub>2</sub> is detected in the depth using a resonant excitation. Raman mapping shows a non-uniform distribution of MoS<sub>2</sub> along the interface between CZTS and back Mo layer.

**Keywords:** CZTS; secondary phase; MoS<sub>2</sub>; Raman mapping; C-AFM

## 1. Introduction

Multicomponent semiconductor  $\text{Cu}_2\text{ZnSnS}_4$  (CZTS) is characterized by direct band gap value of about 1.5 eV, high absorption coefficient ( $10^4$ - $10^5 \text{ cm}^{-1}$  in the visible range), nontoxicity and relative abundance of the initial elements (Ananthoju et al., 2019; Babichuk et al., 2019). Due to those unique features CZTS attracted a scientific attention as a candidate for engineering of high-efficiency, low-cost and radiation-resistant thin film solar cells (TFSCs) (Green et al., 2019; Havryliuk et al., 2018; Temgoua et al., 2019).

Despite the active investigation of CZTS, the role of secondary phases remains unclear. It is known that the existence of the secondary phases in CZTS has a negative influence on the operation of solar cells (Babichuk et al., 2018a; Giraldo et al., 2019b; Scragg et al., 2014). However, it was experimentally concluded that the total  $\text{MoS}_2$  thickness below 200 nm in  $\sim 1 \mu\text{m}$  thick CZTS film was not critical in the functioning of solar cells as a whole (Gao et al., 2018; Yan et al., 2018). Moreover, regardless of the attempts to obtain a perfect material with a good crystal structure (Dobrozhan et al., 2017; Kapush et al., 2015; Pareek et al., 2015), higher power conversion efficiency was detected in the films with disordered structure (Giraldo et al., 2019a; Wang et al., 2014). Indeed, it may not be necessary to suppress the emergence of, e.g.,  $\text{MoS}_2$  secondary phase, but rather control it (Grau et al., 2019).

Modern methods of obtaining thin films allow to precisely control the thickness of the layer. In addition, current methods allow to analyze the film in depth: scanning electron microscopy (SEM) combined with energy dispersive X-ray (EDX) (Yang et al., 2015). In contrast, Raman spectroscopy is commonly used to investigate the surface of bulk and thin films of tetragonal CZTS. Since the interaction of laser excitation with CZTS depends on the absorption coefficient of kesterite (Dimitrievska et al., 2014; Dumcenco and Huang, 2013), Raman spectroscopy became to be an invaluable tool for characterization of secondary phases in CZTS films (Babichuk et al., 2013; Babichuk et al., 2014; Fontané et al., 2012; Sheleg et al., 2014; Valakh et al., 2013a; Valakh et al., 2017). As the light penetration depth into material depends on the

wavelength, there is an ample opportunity for the investigations of CZTS on depth, using lasers of different wavelengths for Raman spectroscopy. It should be noted that, with typical laser sources of excitation in the range from 300 to 500 nm the penetration depth is about a hundred nanometers or less (Dimitrievska et al., 2014). However, while the depth of light absorption in bulk CZTS is relatively the same, this parameter for polycrystalline films is different, resulting in diverse Raman spectra (Salomé et al., 2014). Up to date, the changes optical properties caused by secondary phases in polycrystalline films need further investigation despite the large number of publications dedicated to this question.

In this work we studied the CZTS film prepared by sulfurization of metallic precursors after direct current (DC)-magnetron sputtering. The film was in detail characterized by means of SEM, EDX and  $\mu$ -Raman spectroscopy including mappings. The morphological and structural investigations are focused on depth of the film and interface between the CZTS and back Mo layer. The main goal of this study is to determine the MoS<sub>2</sub> inclusion and its distribution at the CZTS/Mo interface by non-destructive optical method. It is also important to obtain information about other secondary phases both on the surface and in the depth of film and to evaluate their effect on film quality. Within the last task, we have estimated conductivity of the CZTS film using conductive atomic force microscopy (C-AFM).

## **2. Experimental**

The CZTS sample was grown by a two-step process. First, a sequential deposition of the metallic precursor layers was performed by DC magnetron sputtering. The stack ordering was as follows: Mo back contact (1000 nm) / Zn (190 nm) / Cu (150 nm) / Sn (340 nm). Sputtering conditions for the individual metallic precursors were maintained, as it was proposed in (Babichuk et al., 2019; Fernandes et al., 2009). The second stage is the formation of CZTS layer by sulfurization of the precursors. Detailed parameters of a sulfurization chamber were

presented in our previous work (Babichuk et al., 2019). Unlike that work, in this study we used 100 mg instead of 50 mg of S for the sulfurization.

To determine the required amount of S during sulfurization, from the equation for an ideal gas, first we found the change in pressure with temperature by the Arrhenius equation (Wang et al., 2017)

$$\log P = A - \frac{B}{t+C}, \quad (1)$$

where  $P$  is the S vapor pressure (mmHg), and  $t$  is the S temperature ( $^{\circ}\text{C}$ ).  $A$  is = 6.843,  $B$  = 2500.0 and  $C$  = 186.0.

When the S source temperature was at  $550^{\circ}\text{C}$ , the corresponding partial pressure of S vapor was  $3.72 \times 10^5$  Pa. In addition, according to the equation of state of ideal gas  $PV = nRT$ , where  $P$ ,  $V$  and  $T$  are, the S vapor pressure, volume of reactor ( $8.036 \times 10^{-5} \text{ m}^3$ ) and absolute sulfurization temperature (823 K), respectively.  $n$  is the number of S moles.  $R \approx 8.314 \text{ J/(mol}\cdot\text{K)}$  is the ideal gas constant (Caballero et al., 2016). To reach the saturated vapor pressure, the required amount of S powder under  $550^{\circ}\text{C}$  was calculated to be  $4.37 \times 10^{-3} \text{ mol}$ , which was bigger than that of S powder used in this work (the used load of 100 mg corresponds to  $3.125 \times 10^{-3} \text{ mol}$ ). After the sulfurization for 30 min at  $550^{\circ}\text{C}$ , the samples were naturally cooled down to room temperature.

Surface morphology and cross-section of the sample was analyzed by means of SEM with a Hitachi SU8230. The elemental composition was defined by EDX, employing an INCAx-sight Oxford instruments. The EDX measurements were carried out at 20 kV operating voltage and involved Cu K, Zn K, Sn L, S K lines. To determine the composition of formed film and individual phase inclusions, the local EDX studies were performed in various cross-section regions of the film at a fresh sample cleavage. In order to obtain reliable results from the EDX measurements, the system was calibrated using elemental standards. The resolution of EDX bands obtained from the individual elements was found to be satisfactory, despite a relatively high energy of the probe electrons used to obtain the contribution of items from all the cross-

section regions. In this case, it is possible to get more complete information about elemental composition. The cross-section SEM (Fig. 1a) proves that the sample consists of the Mo layer deposited on glass and the CZTS layer above. It should be noted that we could not clearly detect MoS<sub>2</sub> from the cross-section. This may be due to the reason that the thickness of MoS<sub>2</sub> film on the CZTS/Mo interface is less than the resolution of the equipment, or indistinct boundary of MoS<sub>2</sub> with CZTS, which made it impossible to register the contrast.

Topography and local conductivity at the film surface was analyzed by means of conductive AFM exploiting a Dimension 3100 by Bruker. In so doing, a Pt/Ir-coated tip (Nano sensor) was used and bias voltage of 2 V was applied to the surfaces on  $5 \times 5 \mu\text{m}^2$  scanned areas. The Mo layer was used as the back contact connected with a silver paste to a metal-coated conducting probe which was grounded.

A Horiba LabRAM HR Evolution spectrometer and a confocal Raman imaging Alpha300Ri or a HR550 Andor systems with a Newton 920 CCD detector were employed for room temperature Raman spectroscopy and mapping in the backscattering configuration with 325, 532 and 785 nm excitations. The laser beam was focused on the sample surface with a 50x objective of a confocal Olympus microscope to a spot of  $\sim 1 \mu\text{m}$  in diameter. The laser power density did not exceed  $\sim 10^6 \text{ W/cm}^2$  to avoid alterations in the film structure during the sample excitation, as was confirmed earlier (Brus et al., 2016; Havryliuk et al., 2019; Semenenko et al., 2019; Semenenko et al., 2017). Reflection and transmittance measurements were carried out using a spectrophotometer Shimadzu UV-3600.

### **3. Results and discussion**

The surface SEM image (Fig. 1b) show that the CZTS film is granular with the grain size ranges from 0.6 to 1.8  $\mu\text{m}$  and a mean grain size of  $0.8 \pm 0.2 \mu\text{m}$ . These results are in good agreement with the literature data for the films obtained at the same sulfurization time, temperature and pressure (Olgar, 2019; Olgar et al., 2019).

To detect the CZTS film stoichiometry, EDX mapping was performed on the cross-sectional SEM images (Fig. 1c). The data evidence that the S content increases with depth, similar gradient of S was well described in Ref. (Babichuk et al., 2019). Otherwise, the Cu amount decreases towards the bottom, apparently, due to the high diffusion coefficient of Zn in Cu under these conditions of sulfurization (Dutt and Sen, 1979). As for Zn and Sn, these elements reveal negligible dependence on depth. Minor trends with depth, seen in Fig. 1d for these elements, could be related to positions of their precursor layers before the sulfurization (He et al., 2015; Yang et al., 2015).

The comparative estimation of the main elements versus depth, averaging composition over 0.1  $\mu\text{m}$  of thickness, is presented in Fig. 1e. The ratios of  $\text{Cu}/(\text{Zn}+\text{Sn})$ ,  $\text{Zn}/\text{Sn}$  and  $\text{S}/(\text{Cu}+\text{Zn}+\text{Sn})$  are close to 1 from the film surface down to the depth of 0.5  $\mu\text{m}$ , while a deviation from the required parameters is observed below. The  $\text{Cu}/\text{Zn}$  ratio is close to the expectable value of 2 near the surface and shows a significant deviation near the CZTS bottom. This is apparently due to the precursor layer positions before the sulfurization. Since these ratios play an important role in the ordering and phase stability of CZTS, deviations from the stoichiometric values would induce the appearance of defects, different polytypes and secondary phases (Babichuk et al., 2018b; Gurieva et al., 2018; Schorr et al., 2019), which is investigated in detail below.

High conductivity of absorbing film is also an imperative factor for the material consuming in TFSC. Two-dimensional AFM topography spatial map of the CZTS film is shown in Fig. 2a together with the respective local surface current map in Fig. 2b. The one-dimensional current and morphology profile along the a–a' line (Fig. 2c) reveals a high current of  $15 \pm 4.8$  nA and its profile is dense compared to the literature data (Babichuk et al., 2019; Yang et al., 2018; Yang et al., 2015). Integration of the current over the  $5 \times 5 \mu\text{m}^2$  area of measurement allows to estimate arithmetical mean value of current for the film as 6.4 nA. The 3D maps correspond to the 2D ones on Fig. 2a-b and give better understanding of the surface roughness, grain size and local current distribution. Bearing analysis of the distribution of local current was carried out

(Fig. 2f-h) to reveal local surface current values which are above a certain one. The blue color in Fig. 2f-h marks the fractions of the bearing area with current values above the points 20, 15 and 10 nA, respectively. The respective fractions are estimated to be 20, 42 and 61 percent.

Most of the references reported a higher local current flow in vicinity of the grain boundaries rather than at the grain surfaces (Courel et al., 2017; Li et al., 2012; Nadarajah et al., 2020; Yang et al., 2018). Otherwise, the first explicit experimental demonstration of current flow was at the certain regions of grain rather than in the grain boundaries for a solar cell material (Metzger and Gloeckler, 2005). Fig. 2c shows no correspondence of the current peaks to the grain boundaries. So, current flowing may be localized at the boundaries and some regions of the grains that are not distinguishable in AFM images. Furthermore, AFM also could not distinguish boundaries between the grains in the case of a weak relief. However, we still think that predominant local electrical transport in this film occurs along grain boundaries, as grain has a lower electron mobility compared to the surrounding regions (Yang et al., 2018). Thus electrons would preferentially flow in the region adjacent to the grain boundaries, where the conductivity is higher. Anyway, we observe in Fig. 2c and 2e a non-homogeneous highly conductive electrical grid with peaks and valleys. The uniform distribution of electrical conductivity across the adsorber will help to create a pullable uniform electric field for efficient separation of photo-generated carriers and their efficient transport to metal electrodes.

Overall, the EDX data prove appropriate CZTS composition that should result in suitable optical properties of the absorber film. The main role of CZTS layer in TFSCs, is the absorption of light in *p*-region of *p-n*-junction. So, optical bandgap energy ( $E_g$ ), an important parameter of the absorber, was estimated from the reflectance and transmittance spectra (Fig. 3). The absorption coefficient and direct  $E_g$  can be determined under the conditions specified in Ref. (Babichuk et al., 2019). The extrapolation of the linear-like segment of  $(ah\nu)^2$  toward the interception with the energy axis, shown in Fig. 3 (inset), allows to estimate  $E_g = 1.48$  eV. This value is close to the optimum value of  $\sim 1.4$  eV that allows to reach a maximum efficiency of



single-junction solar cell calculated within the Shockley-Queisser model (Shockley and Queisser, 1961).

To investigate the kesterite crystal structure and disordering degree in the formed film, Raman spectroscopy and mapping have been approached. Figure 4a-c shows the Raman spectra at different laser excitation wavelengths. The spectrum in Fig. 4a excited with 532 nm ( $\sim 2.41$  eV) reveals two dominant bands at 288 and 338  $\text{cm}^{-1}$  identified as A symmetry mode, together with the weaker contributions at 253, 274, 347, 353 and 368  $\text{cm}^{-1}$  attributed to E and B modes (Caballero et al., 2014; Valakh et al., 2013b).

It is known that the disordering degree of CZTS structure can be estimated from the intensity ratio between the disordered kesterite phase band at 332  $\text{cm}^{-1}$  and the ordered one at 338  $\text{cm}^{-1}$ ,  $I_{332}/I_{338}$  (Caballero et al., 2014). In our film, this ratio is low (0.059) if comparing with other reported results (Caballero et al., 2014). This means a low content of disordered kesterite phase. A high-quality crystal structure of the obtained film agrees with the FWHM analysis of two dominant bands at 288 and 338  $\text{cm}^{-1}$ , where they are 7 and 5.4  $\text{cm}^{-1}$ , respectively.  $\text{Cu}_{2-x}\text{S}$  and  $\text{Sn}_x\text{S}_y$  secondary phases were not detected using the excitations of 532 nm (Babichuk et al., 2018a; Guc et al., 2020; Stetsenko et al., 2016). Inset of Fig. 4a shows distribution of the  $I_{332}/I_{338}$  ratio on area of  $45 \times 45 \mu\text{m}^2$  obtained by Raman mapping under 532 nm excitation. These data give a qualitative picture of the crystal lattice ordering over a relatively large area compared to the micrometer-large spot used to obtain the spectrum in Fig. 4a. We attribute deviations in the  $I_{332}/I_{338}$  ratio over the surface to the polycrystallinity of film, as the deviation areas are comparable to the grain sizes in Fig. 1b.

Fig. 4b shows the Raman spectra measured under 325 nm excitation in three different areas on the sample (curve 1, 2, 3): the areas 1 and 2 are different points of CZTS, while the area 3 corresponds to uncoated Mo film. At these excitation conditions, Raman spectroscopy becomes extremely sensitive in the detection of even small amount of ZnS in sample, since the energy of 325 nm light ( $\sim 3.82$  eV) is close to the resonance absorption in ZnS ( $E_g = 3.54$  eV for cubic

syngony). It should be noted that, using 325 nm excitation, we study the near-surface layer of CZTS film.

Thus, the spectra excited at 325 nm (Fig. 4b, curve 1) are dominated by an intense band at  $347\text{ cm}^{-1}$  identified as the LO mode characteristic for ZnS phase (Babichuk et al., 2019). As can be seen from curve 2, area 2 also contains ZnS secondary phase. The peak positions are similar to curve 1, but the intensity is less. This may be related to a lower amount of ZnS on the surface or its deeper location (Dimitrievska et al., 2014). This correlates with the distribution of elements on the depth.

The area 3 (Fig. 4b, curve 3) corresponds to Mo uncoated before sulfurization. After sulfurization,  $\text{MoS}_2$  is found in the spectra (Xue et al., 2015). However, this secondary phase is also detected in the areas 1 and 2 (curves 1 and 2), which would mean a near-surface excitation of CZTS. But we should take into account that the penetration depth of light into the film could be increased due to cavities between the grains (Fig. 1b). To clarify the location of the  $\text{MoS}_2$  phase, the excitation light with longer wavelength and, hence, higher penetrability into bulk CZTS should be used.

The resonant excitation condition for  $\text{MoS}_2$  can be realized exciting at 633 nm (relatively close to 1.84 eV corresponding to the direct bandgap) and 785 nm (involves only the indirect transitions above 1.3 eV) (2018; Placidi et al., 2015; Yaremko et al., 2017). To get accurate information from the deeper layers, we carried out a resonant Raman mapping using 785 nm excitation, Fig. 4c shows the Raman spectrum. The bands at 338, 365 and  $376\text{ cm}^{-1}$  are associated with CZTS. The  $330\text{ cm}^{-1}$  band is from the disordered kesterite phase and corresponds to the one at  $332\text{ cm}^{-1}$  in Fig. 4a. This band in the CZTS films is known to be related to intrinsic structural defects, such as antisite  $\text{Zn}_{\text{Cu}}$  and vacancy  $\text{V}_{\text{Cu}}$  (Valakh et al., 2013b). Their surface distribution on our film is shown in the inset of Fig. 4a. It is also known that these defects are numerous in Cu-poor CZTS samples, where all Zn atoms and a half of Cu atoms are statistically distributed on both 2d- and 2c-sites (Valakh et al., 2013b). In our case,

Fig. 1d shows that the amount of Cu decreases towards the film depth from the stoichiometric composition to the poor one, while Zn increases. This might lead to an increase in these defects. Under the near-infrared excitation of 785 nm with deeper penetration, we can detect this increase as a notably higher contribution of the respective band, which is wider and slightly shifted towards lower frequencies relative to the band of  $332\text{ cm}^{-1}$ . Also, the shift can be related to heating (Valakh et al., 2013a).

The most intense bands at  $403$  and  $447\text{ cm}^{-1}$  in Fig. 4c are attributed to  $\text{MoS}_2$  secondary phase (Placidi et al., 2015).

The Raman mapping images of  $45 \times 45\text{ }\mu\text{m}^2$  (Fig. 4e-g), which shows intensities of the bands as the brightness on the maps, correspond to the optical image in Fig. 4d. Fig. 4e reveals that the distribution of ordered kesterite phase is homogeneous on the large area of film, while the distribution of  $\text{MoS}_2$  secondary phase is less uniform (Fig. 4f,g). To better understand this, we analyze the thermodynamic formations of some phases. The  $\text{MoS}_2$  distribution can be associated to the time of the reaction of S with different metals and relative arrangement of the precursor layers.

Indeed, according to standard electrode potentials, Zn is the most reactive ( $\text{Zn}^{2+} + 2\text{e}^- \leftrightarrow \text{Zn} = -0.76\text{ V}$ ), the next is Mo ( $\text{Mo}^{3+} + 3\text{e}^- \leftrightarrow \text{Mo} = -0.2\text{ V}$ ), then Sn ( $\text{Sn}^{2+} + 2\text{e}^- \leftrightarrow \text{Sn} = -0.14\text{ V}$ ) and Cu ( $\text{Cu}^{2+} + 2\text{e}^- \leftrightarrow \text{Cu} = +0.34\text{ V}$ ). However, the sequence of metal layers Mo/Zn/Cu/Sn before sulfurization presumes initial formation of  $\text{SnS}_2$  rather than ZnS. It is natural to assume then almost simultaneous formation of  $\text{Cu}_{2-x}\text{S}$  with ZnS, considering the rapid diffusion of Zn in Cu (Dutt and Sen, 1979).

As for the formation of  $\text{MoS}_2$ , this becomes possible after previous reactions, when S, residual from the initial 100 mg, penetrates deep to react with the bottom Mo. The penetration could be due to voids, which might be formed owing to the quick diffusion of Zn and Cu. Localization of these voids might determine nucleation and formation of the  $\text{MoS}_2$  areas.

We also should take into account the highest absolute standard molar enthalpy of MoS<sub>2</sub> among the detected secondary phases;  $\Delta H_o$ , [kJ/mol] for binary sulfides is –53 for Cu<sub>2</sub>S, –82.4 for SnS<sub>2</sub>, –205.4 for ZnS, and –248.1 for MoS<sub>2</sub> (Babichuk et al., 2014), meaning the highest stability of the last compound. Thus, large absolute values of  $\Delta H_o$  allowed ZnS and MoS<sub>2</sub> not to reduce to atomic state during sulfurization unlike other sulfides (Jung et al., 2017; Li et al., 2015; Seo et al., 2014). This can explain big sizes of characteristic areas of MoS<sub>2</sub> in the images about tens of micrometers. This is much larger than the CZTS grain sizes (Fig. 1b), thus we can conclude that the MoS<sub>2</sub> formation is hardly related to the grain formation. The mechanism of formation and elimination of ZnS and MoS<sub>2</sub> secondary phases was proposed in our previous work (Babichuk et al., 2019). Meanwhile, Grau et al. (Grau et al., 2019) showed an increase in the efficiency of TFSC based on CZTS when controlling formation of MoS<sub>2</sub>. Until now, it was believed that the formation of MoS<sub>2</sub> in sulfurization has a negative influence on the efficiency of solar cell. Therefore, instead of counteracting this formation, it may be better to apply MoS<sub>2</sub> and control its deposition (Ferdaous et al., 2019).

Under this long-wavelength excitation the contribution of MoS<sub>2</sub>-related bands compared to those of kesterite is significantly higher than in the spectra excited with 325 nm irradiation. It is due to the resonant excitation conditions of MoS<sub>2</sub> vibration atoms as well as to the fact that the 785 nm laser has a greater depth of penetration into the film. This allows to reveal a higher amount of MoS<sub>2</sub> phase deeper in the CZTS volume rather than near the surface. So, we can conclude that the main amount of MoS<sub>2</sub> is concentrated near the CZTS/Mo interface, despite the measurements under 325 nm showed a less intensity of the MoS<sub>2</sub>-related bands at uncoated Mo layer (curve 3 in Fig. 4b) than at the CZTS surface (curves 1 and 2). In particular, Raman mapping under 785 nm excitation can detect the distribution of MoS<sub>2</sub> phase on the CZTS/Mo interface. This is a non-destructive method to control the quality of the absorbent layer at each stage of manufacture. However, to specify the thickness of found MoS<sub>2</sub>, additional studies are needed. Based on the already obtained Raman data, we can only declare that the thickness is

above 4 nm (6 monolayers) (Golovynskyi et al., 2020; Scragg et al., 2012; Yaremko et al., 2017).

#### **4. Conclusions**

The CZTS thin film with low disordering degree and good crystal structure has been fabricated by DC-magnetron sputtering. The film is characterized by big grains and suitable elemental composition. The estimated optical bandgap of 1.48 eV is close to the optimum value for single-junction solar cell. Herewith, the film contains ZnS and MoS<sub>2</sub> secondary phases. The main amount of MoS<sub>2</sub> in CZTS is located near its interface to the bottom Mo layer, and the MoS<sub>2</sub> phase distribution on the area is found to be non-uniform. Despite the presence of secondary phases in the film, it was found that polycrystalline grains of tetragonal kesterite have a high-conductivity electrical grid at the grain boundaries.

#### **Conflicts of interest**

There are no conflicts to declare.

#### **Acknowledgements**

This research was supported in part by National Natural Science Foundation of China [61525503/61620106016/61835009/81727804/61722508/61604098]; the United Program of National Natural Science Foundation of China with Shenzhen [U1613212]; (Key) Project of Department of Education of Guangdong Province [2015KGJHZ002/2016KCXTD007]; Guangdong Natural Science Foundation [2014A030312008]; Shenzhen Basic Research Project [JCYJ20170817094728456]; Basic Research Program of the National Academy of Science of Ukraine "Fundamental problems of new nanomaterials and nanotechnology" no. [8/19-N]; and Ministry of Education and Science of Ukraine [19BF051-02].

## References

2018. Renewable Energy Policy Network for the 21st Century, Global Status Report (GSR). Paris, pp. 1-325.
- Ananthoju, B., Mohapatra, J., Bahadur, D., Medhekar, N.V., Aslam, M., 2019. Influence of the  $\text{Cu}_2\text{ZnSnS}_4$  nanoparticles size on solar cell performance. *Sol. Energy Mater. Sol. Cells* 189, 125-132.
- Babichuk, I.S., Golovynskyi, S., Brus, V.V., Babichuk, I.V., Datsenko, O., Li, J., Xu, G.W., Golovynska, I., Hreshchuk, O.M., Orletskyi, I.G., Qu, J.L., Yukhymchuk, V.O., Maryanchuk, P.D., 2018a. Secondary phases in  $\text{Cu}_2\text{ZnSnS}_4$  films obtained by spray pyrolysis at different substrate temperatures and Cu contents. *Mater. Lett.* 216, 173-175.
- Babichuk, I.S., Golovynskyi, S., Caballero, R., Gurieva, G., Datsenko, O.I., Babichuk, I.V., Golovynska, I., Havryliuk, Y.O., Qu, J.L., Schorr, S., Yukhymchuk, V.O., 2018b. Thickness-dependent structural parameters of kesterite  $\text{Cu}_2\text{ZnSnSe}_4$  thin films for solar cell absorbers. *Mater. Lett.* 225, 82-84.
- Babichuk, I.S., Semenenko, M.O., Golovynskyi, S., Caballero, R., Datsenko, O.I., Babichuk, I.V., Li, J., Xu, G., Qiu, R., Huang, C., Hu, R., Golovynska, I., Ganus, V., Li, B., Qu, J., Leon, M., 2019. Control of secondary phases and disorder degree in  $\text{Cu}_2\text{ZnSnS}_4$  films by sulfurization at varied subatmospheric pressures. *Sol. Energy Mater. Sol. Cells* 200, 109915.
- Babichuk, I.S., Yukhymchuk, V.O., Dzhagan, V.M., Valakh, M.Y., Leon, M., Yanchuk, I.B., Gule, E.G., Greshchuk, O.M., 2013. Thin films of  $\text{Cu}_2\text{ZnSnS}_4$  for solar cells: optical and structural properties. *Funct. Mater.* 20(2), 186-191.
- Babichuk, I.S., Yukhymchuk, V.O., Semenenko, M.O., Klyui, N.I., Caballero, R., Hreshchuk, O.M., Lemishko, I.S., Babichuk, I.V., Ganus, V.O., M., L., 2014. Optical and morphological properties of tetragonal  $\text{Cu}_2\text{ZnSnS}_4$  thin films grown from sulphide precursors at lower temperatures. *SPQEO* 17(3), 291-294.

Brus, V.V., Babichuk, I.S., Orletskyi, I.G., Maryanchuk, P.D., Yukhymchuk, V.O., Dzhagan, V.M., Yanchuk, I.B., Solovan, M.M., Babichuk, I.V., 2016. Raman spectroscopy of Cu-Sn-S ternary compound thin films prepared by the low-cost spray-pyrolysis technique. *Appl. Optics* 55(12), B158.

Caballero, R., Condé, V., León, M., 2016. SnS thin films grown by sulfurization of evaporated Sn layers: Effect of sulfurization temperature and pressure. *Thin Solid Films* 612, 202-207.

Caballero, R., Garcia-Llamas, E., Merino, J.M., León, M., Babichuk, I., Dzhagan, V., Strelchuk, V., Valakh, M., 2014. Non-stoichiometry effect and disorder in  $\text{Cu}_2\text{ZnSnS}_4$  thin films obtained by flash evaporation: Raman scattering investigation. *Acta Mater.* 65, 412-417.

Courel, M., Andrade-Arvizu, J.A., Guillén-Cervantes, A., Nicolás-Marín, M.M., Pulgarín-Agudelo, F.A., Vigil-Galán, O., 2017. Optimization of physical properties of spray-deposited  $\text{Cu}_2\text{ZnSnS}_4$  thin films for solar cell applications. *Mater. Des.* 114, 515-520.

Dimitrievska, M., Fairbrother, A., Fontané, X., Jawhari, T., Izquierdo-Roca, V., Saucedo, E., Pérez-Rodríguez, A., 2014. Multiwavelength excitation Raman scattering study of polycrystalline kesterite  $\text{Cu}_2\text{ZnSnS}_4$  thin films. *Appl. Phys. Lett.* 104(2), 021901.

Dobrozhan, O.A., Loboda, V.B., Znamenshchykov, Y.V., Opanasyuk, A.S., Cheong, H., 2017. Structural and Optical Properties of  $\text{Cu}_2\text{ZnSnS}_4$  Films Obtained by Pulsed Spray Pyrolysis. *J. Nano- Electron. Phys* 9(1), 01028-01035.

Dumcenco, D., Huang, Y.-S., 2013. The vibrational properties study of kesterite  $\text{Cu}_2\text{ZnSnS}_4$  single crystals by using polarization dependent Raman spectroscopy. *Opt. Mater.* 35(3), 419-425.

Dutt, M.B., Sen, S.K., 1979. The Diffusion of Zinc in Copper and Silver. *Jpn. J. Appl. Phys.* 18(6), 1025-1029.

Ferdaous, M.T., Shahahmadi, S.A., Chelvanathan, P., Akhtaruzzaman, M., Alharbi, F.H., Sopian, K., Tiong, S.K., Amin, N., 2019. Elucidating the role of interfacial  $\text{MoS}_2$  layer in  $\text{Cu}_2\text{ZnSnS}_4$  thin film solar cells by numerical analysis. *Solar Energy* 178, 162-172.

Fernandes, P.A., Salomé, P.M.P., da Cunha, A.F., 2009. Precursors' order effect on the properties of sulfurized  $\text{Cu}_2\text{ZnSnS}_4$  thin films. *Semicond. Sci. Technol.* 24(10), 105013.

Fontané, X., Izquierdo-Roca, V., Saucedo, E., Schorr, S., Yukhymchuk, V.O., Valakh, M.Y., Pérez-Rodríguez, A., Morante, J.R., 2012. Vibrational properties of stannite and kesterite type compounds: Raman scattering analysis of  $\text{Cu}_2(\text{Fe,Zn})\text{SnS}_4$ . *J. Alloys Compd.* 539, 190-194.

Gao, S., Zhang, Y., Ao, J., Lin, S., Zhang, Z., Li, X., Wang, D., Zhou, Z., Sun, G., Liu, F., Sun, Y., 2018. Tailoring  $\text{Mo}(\text{S,Se})_2$  structure for high efficient  $\text{Cu}_2\text{ZnSn}(\text{S,Se})_4$  solar cells. *Sol. Energy Mater Sol. Cells.* 176, 302-309.

Giraldo, S., Jehl, Z., Placidi, M., Izquierdo-Roca, V., Pérez-Rodríguez, A., Saucedo, E., 2019a. Progress and Perspectives of Thin Film Kesterite Photovoltaic Technology: A Critical Review. *Adv. Mater.* 31(16), 1806692.

Giraldo, S., Placidi, M., Saucedo, E., 2019b. Kesterite: New Progress Toward Earth-Abundant Thin-Film Photovoltaic. Elsevier.

Golovynskyi, S., Irfan, I., Bosi, M., Seravalli, L., Datsenko, O.I., Golovynska, I., Li, B., Lin, D., Qu, J., 2020. Exciton and trion in few-layer  $\text{MoS}_2$ : Thickness- and temperature-dependent photoluminescence. *Appl. Surf. Sci.* 515, 146033.

Grau, S., Giraldo, S., Saucedo, E., Morante, J.R., Llobet, A., Gimbert-Suriñach, C., 2019. Multi-layered photocathodes based on  $\text{Cu}_2\text{ZnSnSe}_4$  absorber and  $\text{MoS}_2$  catalyst for the hydrogen evolution reaction. *J. Mater. Chem. A* 7, 24320-24327.

Green, M.A., Dunlop, E.D., Levi, D.H., Hohl-Ebinger, J., Yoshita, M., Ho-Baillie, A.W.Y., 2019. Solar cell efficiency tables (version 54). *Prog. Photovolt: Res. Appl.* 27(7), 565-575.

Guc, M., Andrade-Arvizu, J., Ahmet, I.Y., Oliva, F., Placidi, M., Alcobé, X., Saucedo, E., Pérez-Rodríguez, A., Johnson, A.L., Izquierdo-Roca, V., 2020. Structural and vibrational properties of  $\alpha$ - and  $\pi$ - $\text{SnS}$  polymorphs for photovoltaic applications. *Acta Mater.* 183, 1-10.

Gurieva, G., Valle Rios, L.E., Franz, A., Whitfield, P., Schorr, S., 2018. Intrinsic point defects in off-stoichiometric  $\text{Cu}_2\text{ZnSnSe}_4$ : A neutron diffraction study. *J. Appl. Phys.* 123(16), 161519.



Havryliuk, Y., Selyshchev, O., Valakh, M., Raevskaya, A., Stroyuk, O., Schmidt, C., Dzhagan, V., Zahn, D.R.T., 2019. Raman study of flash-lamp annealed aqueous  $\text{Cu}_2\text{ZnSnS}_4$  nanocrystals. *Beilstein J. Nanotechnol.* 10, 222-227.

Havryliuk, Y., Valakh, M.Y., Dzhagan, V., Greshchuk, O., Yukhymchuk, V., Raevskaya, A., Stroyuk, O., Selyshchev, O., Gaponik, N., Zahn, D.R.T., 2018. Raman characterization of  $\text{Cu}_2\text{ZnSnS}_4$  nanocrystals: phonon confinement effect and formation of  $\text{Cu}_x\text{S}$  phases. *RSC Adv.* 8(54), 30736-30746.

He, J., Sun, L., Chen, Y., Jiang, J., Yang, P., Chu, J., 2015. Influence of sulfurization pressure on  $\text{Cu}_2\text{ZnSnS}_4$  thin films and solar cells prepared by sulfurization of metallic precursors. *J. Power Sources* 273, 600-607.

Jung, H.R., Shin, S.W., Suryawanshi, M.P., Yeo, S.J., Yun, J.H., Moon, J.H., Kim, J.H., 2017. Phase evolution pathways of kesterite  $\text{Cu}_2\text{ZnSnS}_4$  and  $\text{Cu}_2\text{ZnSnSe}_4$  thin films during the annealing of sputtered Cu-Sn-Zn metallic precursors. *Solar Energy* 145, 2-12.

Kapush, O.A., Trishchuk, L.I., Tomashik, V.N., Tomashik, Z.F., Boruk, S.D., Zynyuk, O.V., 2015. Preparation of concentrated monodisperse colloidal solutions of CdTe nanocrystals. *Russ. J. Inorg. Chem.* 60(10), 1258-1262.

Li, J.B., Chawla, V., Clemens, B.M., 2012. Investigating the Role of Grain Boundaries in CZTS and CZTSSe Thin Film Solar Cells with Scanning Probe Microscopy. *Adv. Mater.* 24(6), 720-723.

Li, M.Y., Shi, Y., Cheng, C.C., Lu, L.S., Lin, Y.C., Tang, H.L., Tsai, M.L., Chu, C.W., Wei, K.H., He, J.H., Chang, W.H., Suenaga, K., Li, L.J., 2015. Epitaxial growth of a monolayer  $\text{WSe}_2$ - $\text{MoS}_2$  lateral p-n junction with an atomically sharp interface. *Science* 349(6247), 524-528.

Metzger, W.K., Gloeckler, M., 2005. The impact of charged grain boundaries on thin-film solar cells and characterization. *J. Appl. Phys.* 98(6), 063701.

Nadarajah, M., Singh, O.P., Gour, K.S., Singh, V.N., 2020. Study of the Electrical Properties of  $\text{Cu}_2\text{ZnSnS}_4$  (CZTS) Thin Film Using Atomic Force Microscopy (AFM) Techniques. *J. Nanosci. Nanotechnol.* 20(6), 3925-3928.

Olgar, M.A., 2019. Optimization of sulfurization time and temperature for fabrication of  $\text{Cu}_2\text{ZnSnS}_4$  (CZTS) thin films. *Superlattices Microstruct.* 126, 32-41.

Olgar, M.A., Bacaksız, E., Tomakin, M., Kucukomeroglu, T., Başol, B.M., 2019. CZTS layers formed under sulfur-limited conditions at above atmospheric pressure. *Mater. Sci. Semicond. Process.* 90, 101-106.

Pareek, D., Balasubramaniam, K.R., Sharma, P., 2015. Synthesis and characterization of bulk  $\text{Cu}_2\text{ZnSnX}_4$  (X: S, Se) via thermodynamically supported mechano-chemical process. *Mater. Charact.* 103, 42-49.

Placidi, M., Dimitrievska, M., Izquierdo-Roca, V., Fontané, X., Castellanos-Gomez, A., Pérez-Tomás, A., Mestres, N., Espindola-Rodriguez, M., López-Marino, S., Neuschitzer, M., Bermudez, V., Yaremko, A., Pérez-Rodríguez, A., 2015. Multiwavelength excitation Raman scattering analysis of bulk and two-dimensional  $\text{MoS}_2$ : vibrational properties of atomically thin  $\text{MoS}_2$  layers. *2D Mater.* 2(3), 035006.

Salomé, P.M.P., Fernandes, P.A., Leitão, J.P., Sousa, M.G., Teixeira, J.P., da Cunha, A.F., 2014. Secondary crystalline phases identification in  $\text{Cu}_2\text{ZnSnSe}_4$  thin films: contributions from Raman scattering and photoluminescence. *J. Mater. Sci.* 49(21), 7425-7436.

Schorr, S., Gurieva, G., Guc, M., Dimitrievska, M., Pérez-Rodríguez, A., Izquierdo-Roca, V., Schnohr, C.S., Kim, J., Jo, W., Merino, J.M., 2019. Point defects, compositional fluctuations and secondary phases in non-stoichiometric kesterites. *J. Phys. Energy.*

Scragg, J.J., Wätjen, J.T., Edoff, M., Ericson, T., Kubart, T., Platzer-Björkman, C., 2012. A Detrimental Reaction at the Molybdenum Back Contact in  $\text{Cu}_2\text{ZnSn}(\text{S,Se})_4$  Thin-Film Solar Cells. *J. Am. Chem. Soc.* 134(47), 19330-19333.

Scragg, J.J.S., Choubrac, L., Lafond, A., Ericson, T., Platzer-Björkman, C., 2014. A low-temperature order-disorder transition in  $\text{Cu}_2\text{ZnSnS}_4$  thin films. *Appl. Phys. Lett.* 104(4), 041911.

Semenenko, M., Babichuk, I.S., Khatsevich, I., Antonin, S., Datsenko, O.I., Golovynskyi, S., Evtukh, A., Li, B., Qu, J., 2019. Red-shifted photoluminescence and gamma irradiation stability of “micromorph” (nc-Si/SiO)/DLC down-converter anti-reflection coatings. *Diam. Relat. Mater.* 100, 107578.

Semenenko, M.O., Babichuk, I.S., Kyriienko, O., Bodnar, I.V., Caballero, R., Leon, M., 2017. RF Electromagnetic Field Treatment of Tetragonal Kesterite CZTSSe Light Absorbers. *Nanoscale Res. Lett.* 12(1), 408-415.

Seo, D., Kim, C., Oh, E., Hong, C.W., Kim, J.H., Lim, S., 2014. Control of metal salt ratio and  $\text{MoS}_2$  layer thickness in a  $\text{Cu}_2\text{ZnSnS}_4$  thin film solar cell. *J. Mater. Sci: Mater. Electron* 25(8), 3420-3426.

Sheleg, A.U., Hurtavy, V.G., Mudryi, A.V., Valakh, M.Y., Yukhymchuk, V.O., Babichuk, I.S., Leon, M., Caballero, R., 2014. Determination of the Structural and Optical Characteristics of  $\text{Cu}_2\text{ZnSnS}_4$  Semiconductor Thin Films. *Semiconductors* 48(10), 1296-1302.

Shockley, W., Queisser, H.J., 1961. Detailed Balance Limit of Efficiency of p-n Junction Solar Cells. *J. Appl. Phys.* 32(3), 510-519.

Stetsenko, M.O., Voznyi, A.A., Kosyak, V.V., Rudenko, S.P., Maksimenko, L.S., Serdega, B.K., Opanasuk, A.S., 2016. Plasmonic Effects in Tin Disulfide Nanostructured Thin Films Obtained by the Close-Spaced Vacuum Sublimation. *Plasmonics* 12(4), 1213-1220.

Temgoua, S., Bodeux, R., Naghavi, N., 2019. Influence of the annealing atmosphere and precursor's thickness on the properties of CZTSSe based solar cells. *Sol. Energy Mater. Sol. Cells* 191, 123-132.

Valakh, M.Y., Dzhagan, V.M., Babichuk, I.S., Fontane, X., Perez-Rodriguez, A., Schorr, S., 2013a. Optically induced structural transformation in disordered kesterite  $\text{Cu}_2\text{ZnSnS}_4$ . *JETP Lett.* 98(5), 255-258.

Valakh, M.Y., Kolomys, O.F., Ponomaryov, S.S., Yukhymchuk, V.O., Babichuk, I.S., Izquierdo-Roca, V., Saucedo, E., Perez-Rodriguez, A., Morante, J.R., Schorr, S., Bodnar, I.V., 2013b. Raman scattering and disorder effect in  $\text{Cu}_2\text{ZnSnS}_4$ . *Phys. Status Solidi RRL* 7(4), 258-261.

Valakh, M.Y., Yukhymchuk, V.O., Babichuk, I.S., Havryliuk, Y.O., Parasyuk, O.V., Piskach, L.V., Litvinchuk, A.P., 2017. Vibrational spectroscopy of orthorhombic  $\text{Cu}_2\text{ZnSiS}_4$  single crystal: Low-temperature polarized Raman scattering and first principle calculations. *Vib. Spectrosc.* 89, 81-84.

Wang, W., Wang, G., Chen, G., Chen, S., Huang, Z., 2017. The effect of sulfur vapor pressure on  $\text{Cu}_2\text{ZnSnS}_4$  thin film growth for solar cells. *Solar Energy* 148, 12-16.

Wang, W., Winkler, M.T., Gunawan, O., Gokmen, T., Todorov, T.K., Zhu, Y., Mitzi, D.B., 2014. Device Characteristics of CZTSSe Thin-Film Solar Cells with 12.6% Efficiency. *Adv. Energy Mater.* 4(7), 1301465.

Xue, Y., Zhang, Y., Liu, Y., Liu, H., Song, J., Sophia, J., Liu, J., Xu, Z., Xu, Q., Wang, Z., Zheng, J., Liu, Y., Li, S., Bao, Q., 2015. Scalable Production of a Few-Layer  $\text{MoS}_2/\text{WS}_2$  Vertical Heterojunction Array and Its Application for Photodetectors. *ACS Nano* 10(1), 573-580.

Yan, C., Huang, J., Sun, K., Johnston, S., Zhang, Y., Sun, H., Pu, A., He, M., Liu, F., Eder, K., Yang, L., Cairney, J.M., Ekins-Daukes, N.J., Hameiri, Z., Stride, J.A., Chen, S., Green, M.A., Hao, X., 2018.  $\text{Cu}_2\text{ZnSnS}_4$  solar cells with over 10% power conversion efficiency enabled by heterojunction heat treatment. *Nat. Energy.* 3(9), 764-772.

Yang, K.-J., Kim, S., Sim, J.-H., Son, D.-H., Kim, D.-H., Kim, J., Jo, W., Yoo, H., Kim, J., Kang, J.-K., 2018. The alterations of carrier separation in kesterite solar cells. *Nano Energy* 52, 38-53.

Yang, K.-J., Sim, J.-H., Son, D.-H., Kim, D.-H., Kim, G.Y., Jo, W., Song, S., Kim, J., Nam, D., Cheong, H., Kang, J.-K., 2015. Effects of the compositional ratio distribution with sulfurization temperatures in the absorber layer on the defect and surface electrical characteristics of  $\text{Cu}_2\text{ZnSnS}_4$  solar cells. *Prog. Photovolt: Res. Appl.* 23(12), 1771-1784.

Yaremko, A.M., Yukhymchuk, V.O., Romanyuk, Y.A., Baran, J., Placidi, M., 2017. Theoretical and Experimental Study of Phonon Spectra of Bulk and Nano-Sized  $\text{MoS}_2$  Layer Crystals. *Nanoscale Res. Lett.* 12(1), 82.

## Figure captions

**Figure 1.** Cross-section (a) and surface morphology (b) SEM images, EDX element mapping (c) together with compositional distributions (d) and ratios between elements versus depth (e) of the CZTS film sulfurized at 50 mbar.

**Figure 2.** C-AFM morphology image of the CZTS film (a) and respective local current map obtained at a sample bias of 2 V (b) as well as relief and current topography along the line a-a' (c). The 3D plots of morphology (d) and current map (e) are also shown, as well as the bearing areas with current values above 20 (f), 15 (g), and 10 nA (h), marked in blue.

**Figure 3.** Reflectance and transmittance spectra of the studied film. Inset: resulting absorption spectrum as  $(ah\nu)^2 = f(h\nu)$  and  $E_g$  estimation (in the inset).

**Figure 4.** (a)  $\mu$ -Raman spectrum (532 nm excitation) of the CZTS film and also fitted with Lorentz's functions and the distribution of  $I_{332}/I_{338}$  ratio on area of  $45 \times 45 \mu\text{m}^2$  (inset); (b)  $\mu$ -Raman spectra at 325 nm excitation in different points indicated in the surface optical microscopy image  $200 \times 200 \mu\text{m}$  (inset); (c)  $\mu$ -Raman spectra at 785 nm excitation; (d) optical image of the CZTS film and its confocal Raman mapping over areas of  $45 \times 45 \mu\text{m}^2$  with resolution of  $4.5 \mu\text{m}$  for the bands at 338 (e), 403 (f), and  $447 \text{ cm}^{-1}$  (g).

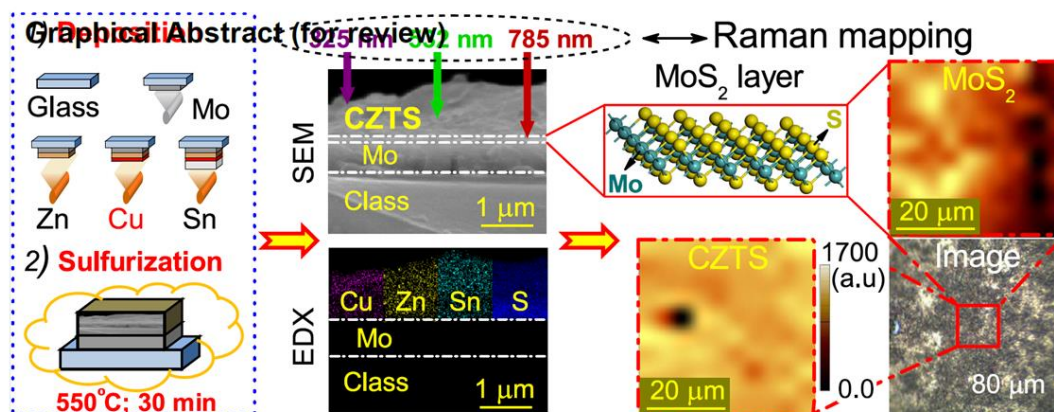


Figure 1

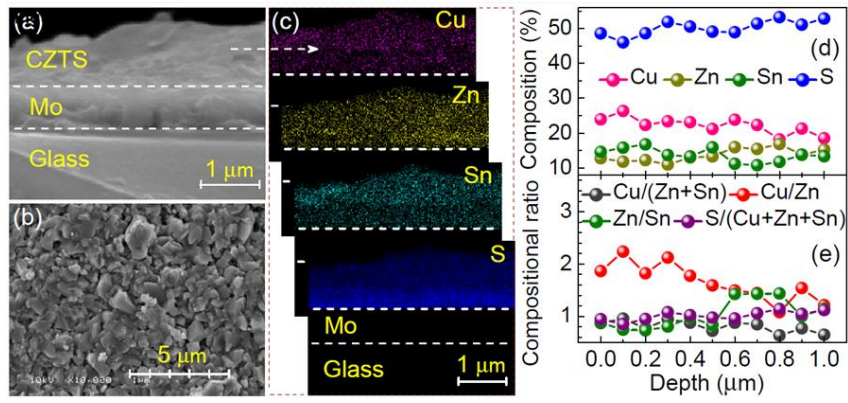




Figure 2

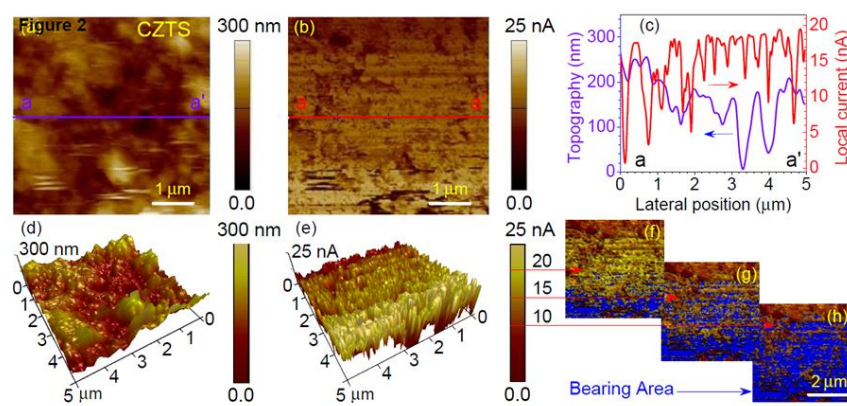


Figure 3

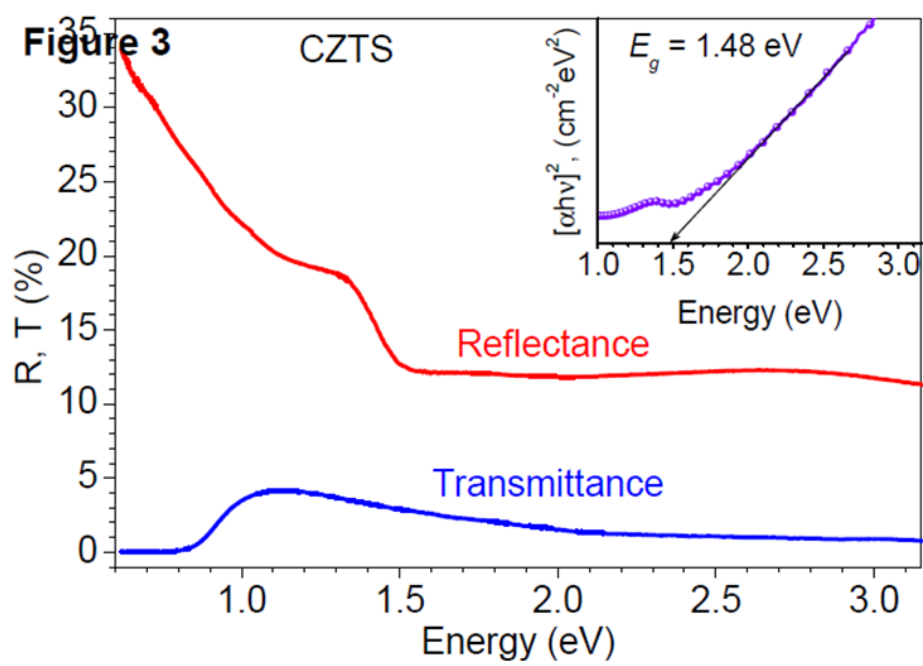


Figure 4

